Analyst

A Modular Microscopic Smartphone Attachment for Imaging and Quantification of Multiple Fluorescent Probes Using Machine Learning

Journal:	*Analyst*
Manuscript ID	AN-ART-12-2020-002451.R1
Article Type:	Paper
Date Submitted by the Author:	08-Mar-2021
Complete List of Authors:	Sami, Muhammad; Rutgers The State University of New Jersey, Tayyab, Muhammad ; Rutgers The State University of New Jersey Parikh, Priya ; Rutgers The State University of New Jersey Govindaraju, Harshitha ; Rutgers The State University of New Jersey Hassan, Umer; Rutgers The State University of New Jersey, Electrical and Computer Engineering

A Modular Microscopic Smartphone Attachment for Imaging and Quantification of Multiple Fluorescent Probes using Machine Learning

Muhammad A. Sami[1], Muhammad Tayyab[1], Priya Parikh[1], Harshitha Govindaraju[2], Umer Hassan*[1, 3]

[1] Department of Electrical and Computer Engineering, School of Engineering, Rutgers The State University of New Jersey, Piscataway, NJ, USA

[2] Department of Biomedical Engineering, School of Engineering, Rutgers The State University of New Jersey, Piscataway, NJ, USA

[3] Global Health Institute, Rutgers The State University of New Jersey, New Brunswick, NJ, USA

*Corresponding Author: umer.hassan@rutgers.edu; Tel (848) 445-2164

Abstract

Portable smartphone-based fluorescent microscopes are becoming popular owing to their ability to provide major functionalities offered by regular benchtop microscopes at a fraction of the cost. However, smartphone-based microscopes are still limited to a single fluorophore, fixed magnification, the inability to work with a different smartphones, and limited usability to either glass slides or cover slips. To overcome these challenges, here we present a modular smartphone-based microscopic attachment. The modular design allows the user to easily swap between different sets of filters and lenses, thereby enabling utility of multiple fluorophores and magnification levels. Our microscopic smartphone attachment can also be used with different smartphones and was tested with Nokia Lumia 1020, Samsung Galaxy S9+, and an iPhone XS. Further, we showed imaging results of samples on glass slides, cover slips, and microfluidic devices. A 1951 USAF resolution test target was used to quantify the maximum resolution of the microscope which was found to be 3.9 μm. The performance of the smartphone-based microscope was compared with a benchtop microscope and we found an R^2 value of 0.99 using polystyrene beads and blood cells isolated from human blood samples collected from Robert Wood Johnson Medical Hospital. Additionally, to count the particles (cells and beads) imaged from the smartphone-based fluorescent microscope, we developed artificial neural networks (ANNs) using multiple training algorithms, and evaluated their performances compared to the control (ImageJ). Finally, we did ANOVA and Tukey's post-hoc analysis and found a p-value of 0.97 which shows that no statistical significant difference exists between the performance of the trained ANN and control (ImageJ).

Key Words: Smartphone based microscope, Fluorescent microscopy, Artificial Neural Networks, Fluorescent beads, Peripheral blood leukocytes. Statistical analysis, ANOVA, Tukey's test.

Introduction

Modern laboratories are equipped with a wide range of analytical instruments. Among these, fluorescent microscopes are of particular importance, especially in the fields of biology and material science [1,2]. They enable identification of cells and cellular components with a high precision. By tagging the specimen with multiple different probes, fluorescent microscopy can simultaneously identify several target molecules[3,4]. In addition to fluorescent microscopes, other benchtop instruments, such as flow cytometers and hematology analyzers are also heavily utilized in clinical laboratories for the purpose of disease diagnosis and patient prognosis by analyzing various biomarkers in clinical samples such as whole blood. In particular, both flow cytometers and hematology analyzers are used for various blood cells enumeration and their membrane antigens quantification. These measurements are routinely monitored in the hospitals for a variety of diseases, especially patient stratification with infectious diseases. Though these modern devices are extremely precise and equipped with a lot of functional modalities, they are highly expensive (e.g., cost thousands of dollars), lacks portability and require trained personnel to operate. Recently, researchers have developed multiple smartphone-based biosensors to provide low cost, portable, and efficient alternatives to the traditional bulky benchtop instruments found in lab settings[5].

Smartphone-based fluorescent microscopes (SBFMs) have a great potential to be used as point of care platforms for diagnostics, healthcare, and environmental monitoring[6]. Modern smartphones are equipped with cutting edge camera units which allow to capture high quality images. SBFMs have been employed in a wide range of settings that include the detection of different biomarkers including proteins and nucleic acids[7-11]. Ozcan et.al reported the quantification of red and white blood cells as well as hemoglobulin from whole blood using a smartphone-based microscope[12]. Moreover, SBFMs have also been employed for the detection of parasites[13] as well as imaging the nanoparticles and viruses[14]. The design and working of a multi color smartphone-based fluorescence microscope capable of imaging two fluorophores at two magnification levels has been demonstrated[15]. Researchers have also reported the use of colored lenses along with smartphones to image multiple fluorophores[16]. SBFMs have also been used for monitoring drug-induced nephrotoxicity on an organ on chip (OOC) platform[17]. Lee et al.[18] demonstrated the adaptation of a smartphone's camera to function as a compact lens less microscope in ambient light. The method is based on the shadow imaging technique where the sample is placed on the surface of the image sensor, which captures direct shadow images under illumination. A hand-held smartphone based quantitative phase

microscopy employing transport of intensity equation method has also been demonstrated[19]. Jung et al.[20] presented a portable multi-contrast microscope operating on a smartphone platform. Based on color-multiplexing of illumination angles, the microscope enabled acquisition of bright field, dark field, and differential phase contrast images in a single shot. Identification of fluorescently labelled pathogenic bacteria has been recently demonstrated using a SBFM[21]. Knowlton et al.[22] developed a SBFM incorporating magnetic focusing technology to increase the application of the platform to a broad range of biomedical assays. Shan et al.[23] developed a fluorescent microscope for on-site quantitative Hg^{2+} measurement based on a fluorescent biosensor. Recently, a smartphone-based fluorescent microscope with a hydraulically driven optofluidic lens was used for the quantification of glucose with high accuracy[24]. Another smartphone-based microscope employed deep learning for the automated screening of sickle cells[25]. Fresh tissue samples have been imaged at cellular resolution using smartphone-based epifluorescence microscopy[26]. Another recently published study reported the use of a smartphone-based microscope for the detection of norovirus in water samples with high precision[27]. Another smartphone-based particle counting platform was recently reported as an alternative to bulky laboratory-based flow cytometers and hematology analyzers[28]. In our past studies, we have also used a biochip in conjunction with SBFMs for quantification of nCD64 and leukocytes at the POC[29,30].

Many challenges remain to develop an ideal SBFM capable of mimicking the functionality of a benchtop microscope by allowing the imaging of multiple fluorophores and offering the user different levels of magnifications. In addition, with more than 1.5 billion new smartphones getting sold every year[31] with significantly different imaging models and camera settings, SBFMs should be generic in nature and not limited to a single device. Furthermore, they should offer compatibility with microfluidic devices and not just limited to imaging specimens on a glass slide. To the best of our knowledge, no such SBFM has yet been reported which satisfies all the above-mentioned criteria.

In this article, we present the design and working of a modular SBFM that satisfies the criteria mentioned above. Our SBFM is capable of working with a multitude of smartphones. The lens used for creating the necessary magnification and the filters employed for creating the necessary darkfield image are all easily swappable. This allows our SBFM to work with multiple fluorophores and capture images at multiple magnification levels as desired by the user. We have imaged human peripheral blood leukocytes and

polystyrene beads tagged with green and red fluorophores using our setup at two different magnification levels. Furthermore, to automate the quantification process of the imaged beads and leukocytes, we developed a machine learning model based on an artificial neural network (ANN). The ANN was trained through multiple training algorithms and its performance was compared to the particle counts obtained from the control (ImageJ). Lastly, we performed statistical analysis to determine if there was a statistically significant difference between the counts predicted from the ANN based algorithm and the control.

Materials and methods

Resolution quantification:

A 1951 USAF resolution test chart from Edmund optics (Catalog # R1DS1P) was used to measure the resolution of the designed SBFM. Samsung Galaxy S9+ and Nokia Lumia 1020 were used along with lens (focal length= 10 mm) and the resolution test chart was imaged using both smartphones. Pixel intensities of the obtained images were analysed by using ImageJ to quantify the resolution of the SBFM when used in conjunction with each of these devices. A target in the test chart was deemed resolvable if the corresponding pixel intensity peaks obtained from its image were clearly distinguishable.

Green fluorescent bead imaging on SBFM:

Green fluorescent microbeads with a mean diameter of 8.3 μm were acquired from Banglabs (Product # UMDG003). These specific beads were chosen because they are comparable in size to human lymphocytes (smaller diameter leukocytes). A long pass filter with a cut-off value of 500 nm was used along with lens A (15 mm focal length) for imaging. Different concentrations of these beads were prepared by adding them in 1X PBS buffer. Subsequently, a 2 μl sample with varying concentrations of microbeads was placed inside the smartphone setup for imaging. The fluorescent beads were excited using the light emitted by the smartphone setup's blue LED's and imaged by a Samsung Galaxy S9+ used in conjunction with lens A (15 mm focal length) and 500 nm long pass filter.

Red fluorescent bead imaging on SBFM:

Red fluorescent microbeads with a mean diameter of 10 μm were acquired from Thermofisher Scientific (Catalog # F8834). To image red fluorescent beads, a long pass filter with a cut-off value of 593 nm was used along with lens A (15 mm focal length). Different concentrations of these beads were prepared by

adding them in 1X PBS buffer. Subsequently, a 2 µl sample with varying concentrations of microbeads was placed inside the smartphone setup for imaging. The fluorescent beads were excited using the light emitted by the smartphone setup's green LED's and imaged by a Samsung Galaxy S9+ used in conjunction with lens A (15 mm focal length) and 593 nm long pass filter.

Human subject statement:

Human blood samples were obtained from anonymous patients at Robert Wood Johnson Medical Hospital. The blood samples were de-identified by the hospital staff before providing to investigators. Our study is approved by Institutional Review Board (IRB) at Rutgers, The State University of New Jersey and Robert Wood Johnson Medical Hospital (IRB application # Pro2018002356). All experiments in the current study were performed in accordance with the IRB protocol ethical guidelines. Patients were selected for whom a lactate test was ordered, and we were provided de-identified left-over blood samples which didn't require the informed consent in accordance with the IRB guidelines.

Preparation of leukocytes for fluorescent imaging:

100 µl of whole blood was poured in a 15 ml conical centrifuge tube. 1 ml RBC lysis media (ThermoFisher scientific, Cat. #: 00-4333-57) was added to whole blood and mixed gently by pipetting. This solution was then incubated at 25°C for 10 minutes to lyse the red blood cells present in the sample. After 10 minutes, 2 ml of 1X PBS was added into the mixture to stop the lysing process. The mixture was then centrifuged at 300g for 5 minutes. The supernatant was then removed from the centrifuge tube by pipetting and a palette of leukocytes was left behind. These leukocytes were then resuspended in RPMI 1640 Medium from ThermoFisher Scientific (Catalog number: 11875085) and were gently stirred to get a uniform concentration.

A green nuclear stain was used to make these isolated leukocytes fluoresce for imaging and counting purposes. Stock solution for the nuclear stain was prepared by adding 3 µl of SYTO 16, (ThermoFisher Scientific, Catalogue Number: S7578), in 1 ml of 1X PBS. SYTO 16 stock solution and the isolated leukocytes were then added in a 1:1 ratio in a 1.5 ml Eppendorf tube and were incubated in dark for 15 minutes at room temperature. The leukocyte isolation process from whole blood is shown in **Figure 1**.

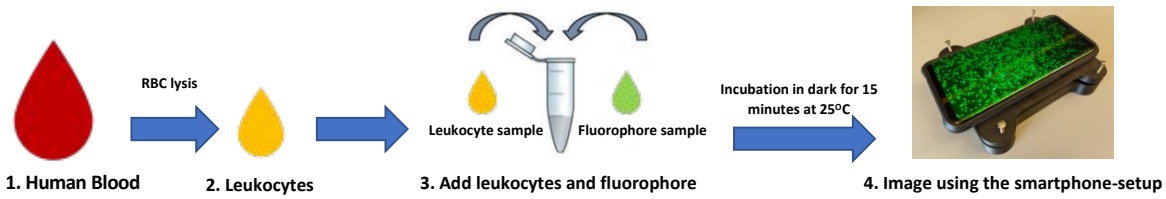

Figure 1: Flowchart explaining the protocol for leukocyte isolation from whole blood and the addition of nuclear stain for fluorescent imaging.

Benchtop fluorescent microscope:

Images of the different bead and leukocyte concentrations were also imaged using Olympus IX81 fluorescent microscope with a 465-495 nm excitation and 515-555 nm emission filters. These images were used as a control for comparison with the SBFM's images to verify the accuracy of the SBFM.

Leukocyte and bead quantification using ImageJ:

ImageJ was used a control method for quantifying the beads and leukocytes imaged through the SBFM. The obtained images were first converted into 8-bit format and then the thresholding function in ImageJ was used to encapsulate the regions of interest. The pixel size and the circularity range are then provided to get the final count. Because leukocytes are not completely round, the circularity was kept in a range of 0.6 to 1, where 1 represents a perfect circle. The flowchart shown in **Figure S1** represents the steps involved in getting a particle count from an image using ImageJ.

Leukocyte and bead quantification using artificial neural networks (ANN):

MATLAB was used to develop the image processing algorithm for quantifying the particles (leukocytes and beads) in the images obtained using the SBFM. The developed algorithm is based on the *imfinddcircles()* function of MATLAB and takes in the size range of particles to be quantified. First, we generated 10 possible counts for sensitivity values ranging from 0.87- 0.96. Multivariate regression was performed on this data using artificial neural networks in MATLAB. The network diagram of the double layer feed forward artificial neural network with sigmoid neurons and softmax output is shown in **Figure S2**. The designed neural network consisted of 10 neurons (hidden layer) and 1 neuron (output layer). The input to the neural network contained the 10 counts generated earlier using sensitivity values from 0.87 to 0.96. For training the neural network, 93 SBFM images were used, and their particle counts are listed in **Table S1**. This network was then trained using three different training methods. For each training method, ten different networks were

created resulting in a net total of 30 networks. The flowchart given in **Figure S3** outlines the process of determining counts from SBFM images using the developed ANN.

Statistical analysis:

Three artificial neural networks were selected with highest accuracy and their counts were compared to the control counts (ImageJ) to determine if there exists a statistically significant difference between them. First, Shapiro-Wilks test was applied on each data set to determine its normality. Bartlett's test was then used to determine if there was any significant difference between the variances of the data sets. ANOVA was also used to determine if a statistically significant difference existed among the data sets. For post-hoc analysis, Tukey's test was used to determine if individual differences existed between each data set. A significance level of ($\alpha = 0.05$) was used. These statistical analyses were carried out using R.

Design of smartphone-based fluorescent microscope:

A 3D CAD model of the smartphone-based fluorescent microscope was made using SolidWorks 2016. The smartphone-based microscope consists of two main parts, the bottom and the top portion as shown in **Figure 2A**. The bottom portion contains two cavities, one for the imaging of fluorescent samples and the other for placement of batteries. Additionally, the bottom portion also contains two openings for the placement of LED's which are used for fluorescent excitation. Each opening contains a set of three individual LED's, one is green and the other is blue in colour. Blue LED's, (Product no: 516-2800-1-ND) were purchased from Digi Key corporation and green LED's from Adafruit (Product ID: 300). A bandpass filter with a centre wavelength of 470 nm and bandwidth of ~40 nm (Chroma Inc, Product no. ET470/40x) is used as an excitation filter for blue LED's. However, for green LED's, a bandpass filter with 535 nm centre wavelength and bandwidth of 50 nm (Chroma Inc., Product no. ET535/50m) is used. As shown in **Figure 2B**, the top portion of the microscope contains a slot for the placement of the lens which works in conjunction with the smartphone lens to form relay lens system, thus, creating the necessary magnification for imaging. Two lenses with different focal lengths were procured from Edmund optics which can be used interchangeably depending on the magnification and field of view (FOV) requirements. Lens A (Edmund optics, Stock #27-691), with 15mm focal length offers a bigger FOV but lesser magnification compared to lens B (Edmund optics, Stock #45-208), which has a 10 mm focal length. Since these lenses have different diameters, they

are first placed in their individual lens holders which makes it possible to use them with the same top portion. For adjusting the depth of focus, 4 screws were placed in the top portion which can be manually rotated to adjust the depth of focus of the microscope as shown in **Figure 2C**. Furthermore, the top portion also contains the slot for the placement of excitation filter which can be easily replaced corresponding to the type of fluorophore being use. In case of green fluorophores, a long pass filter with a cut-off value of 500 nm (Semrock, Product no: FF01-500/LP-23.3-D) is used, whereas, in case of red fluorophores, a long pass filter with a cut-off value of 593 nm (Semrock, Product no: FF01-593/LP-25) is used. To further improve the quality of the created dark field, a cover shield is used, which minimizes the amount of excitation light getting through to the camera sensor. The designed microscopic smartphone attachment was 3D printed (Markforged, Mark two) using Onyx thermoplastic material.

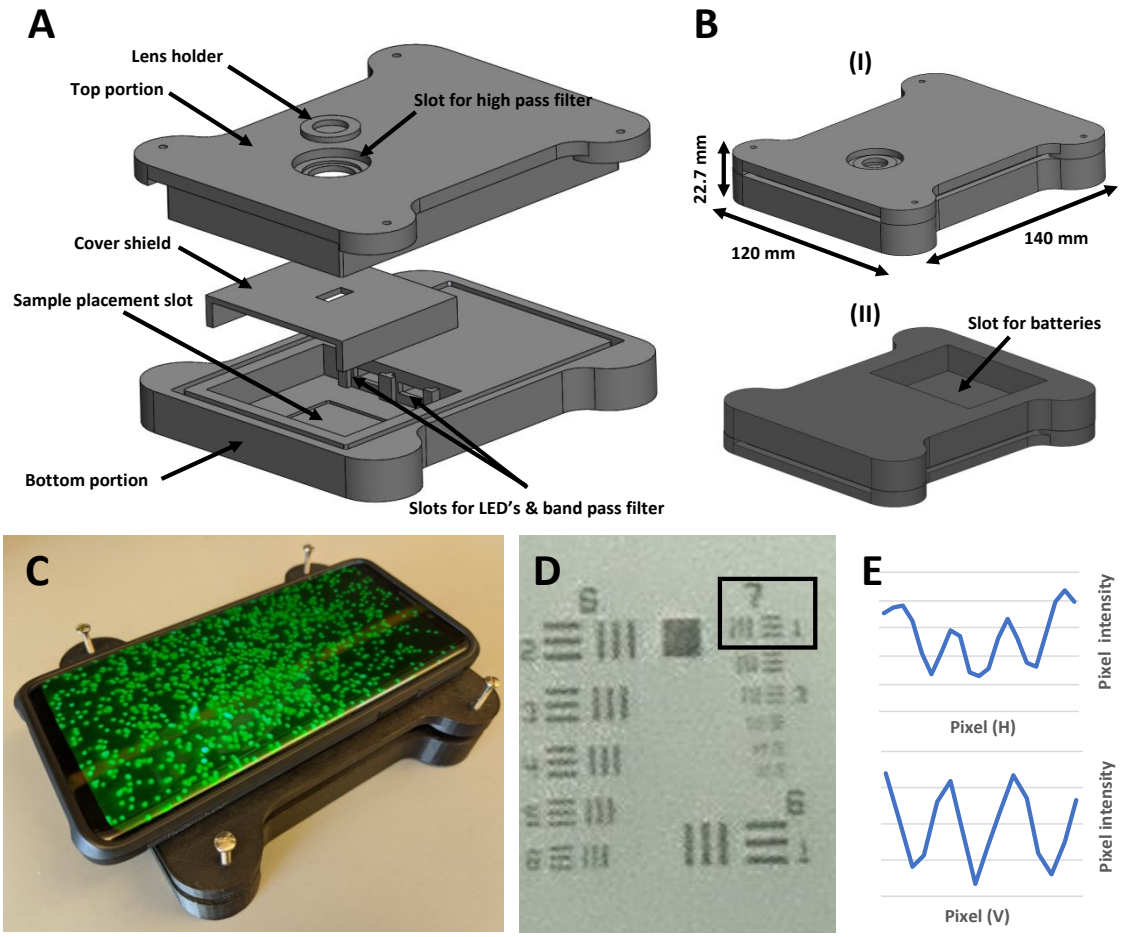

Figure 2: (A) Disbanded 3D CAD Model of the designed microscopic SBFM, (B) (I) Dimensions of the SBFM, (II) Underside of the bottom portion with battery slot, (C) 3D printed SBFM with Samsung Galaxy S9+. (D) 1951 USAF resolution test chart imaged from the SBFM using Lumia 1020. (E) The pixel intensity plots of Group 7 element 1 showing a resolution of 3.9 µm.

Results

Multiple smartphone options offered by SBFM:

The SBFM is generic in nature and can be used with a multitude of smartphones. For the purpose of this study, a Samsung Galaxy S9+ was used to conduct the fluorescent beads and leukocytes quantification experiments. Lumia 1020 and an iPhone XS were used for checking the capability of our SBFM to handle smartphones from different companies. We found the performance of the SBFM to be satisfactory with all of the aforementioned smartphones. The images taken from Lumia 1020 and iPhone XS can be seen in **Figure S4**. No manual adjustments need to be made in the SBFM when switching between different smartphones for imaging. The user can easily switch between smartphones and simply place the smartphone of choice on top of the SBFM and start taking images with the new smartphone immediately.

Optical resolution:

Nokia Lumia 1020 and Samsung Galaxy S9+ were both used to quantify the spatial resolution of the designed SBFM. Lumia 1020 has an internal lens of 7.2 mm focal length and Galaxy S9+ uses a 4.3 mm one. When used in conjunction with Lens B (10 mm focal length), Lumia 1020 and Galaxy S9+ offer magnification ratios equal to 0.72 and 0.43, respectively. The 1951 USAF resolution test chart imaged from Lumia 1020 is shown in **Figure 2D**. Pixel intensities of vertical and horizontal lines of Group 7 element 1 shown in Figure 2e point to a maximum spatial resolution of 3.9 um for the SBFM when used with Lumia 1020. **Figure S5** shows the 1951 USAF resolution test chart when imaged from Galaxy S9+. Pixel intensities of vertical and horizontal lines of Group 6 element 3 point to a maximum spatial resolution of 6.2 um for the SBFM when used with Galaxy S9+.

Multiple magnification options offered by SBFM:

The images of green and red fluorophores particles were obtained with our SBFM by using the protocols mentioned earlier and are shown in **Figure 3**. The only manual adjustment required in the setup will be when a user would like to swap a lens to get a different magnification for a different target application. This will require a single time manual adjustment of the SBFM to focus the image on smartphone by simply rotating the 4 screws shown in Figure 2C. Once the calibration is done for a specific lens, multiple images can be taken using any smartphone of choice by placing the smartphone on top of the SBFM and simply clicking the capture button of the camera app. Any user with our fixed setup will not perform any manual adjustments

to take images. We also verified the multiple magnification feature of the SBFM by swapping lens A with lens B and imaging the samples at the maximum magnification offered by each lens. **Figures 3A** and **3B** show the maximum magnification offered by SBFM when lens A is being used, while **Figures 3C** and **3D** show the maximum available magnification when particles were imaged using lens B.

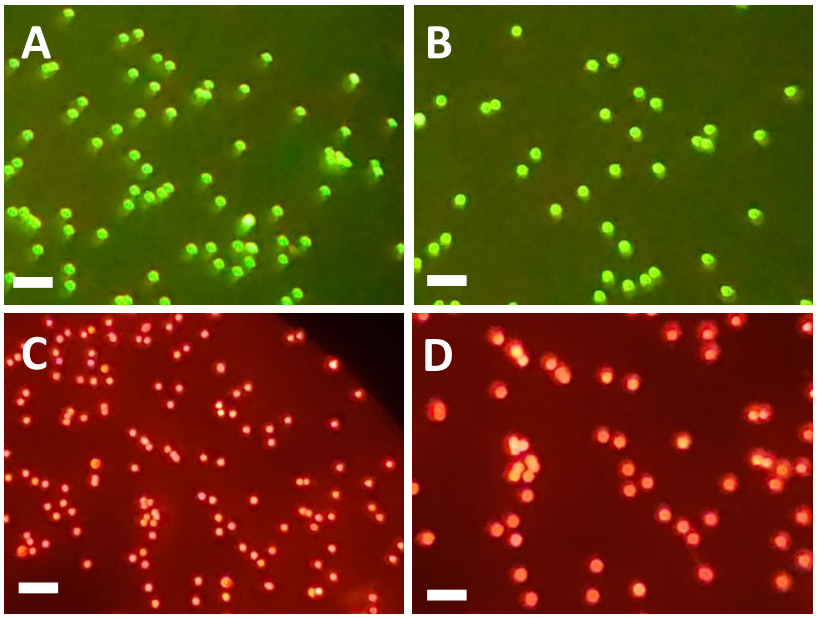

Figure 3: (A) Green fluorescent particles imaged with SBFM using lens A and Galaxy S9+. (B) Green fluorescent particles imaged with SBFM using lens B and Galaxy S9+. (C) Red fluorescent particles imaged with SBFM using lens A and Galaxy S9+. (D) Red fluorescent particles imaged with SBFM using lens B and Galaxy S9+ . (Scale bars (A, C) = 50μm; Scale bars (B, D) = 30μm)

Imaging performance of proposed SBFM:

Green fluorescent beads were imaged by using both smartphone-based microscope and a benchtop fluorescent microscope. **Figure 4A** shows the beads imaged by the smartphone-based microscope and **Figure 4**B shows the beads when imaged under a laboratory benchtop fluorescent microscope. SYTO 16 tagged leukocytes imaged using the smartphone-based and benchtop microscopes are shown in **Figure 4C** and **Figure 4D** respectively. Red fluorescent beads were also imaged by using both the SBFM and a benchtop fluorescent microscope and are shown in **Figure 4E** and **Figure 4F** respectively. ImageJ was used to analyze these images to find the particle count and a good correlation was found between the smartphone and microscope counts with an $R^2 = 0.99$ as shown in **Figure 4G**. The Bland-Altman analysis of the data is shown in **Figure 4H.** Bias value obtained is 10 and limits of agreement are (40.65, -20.65).

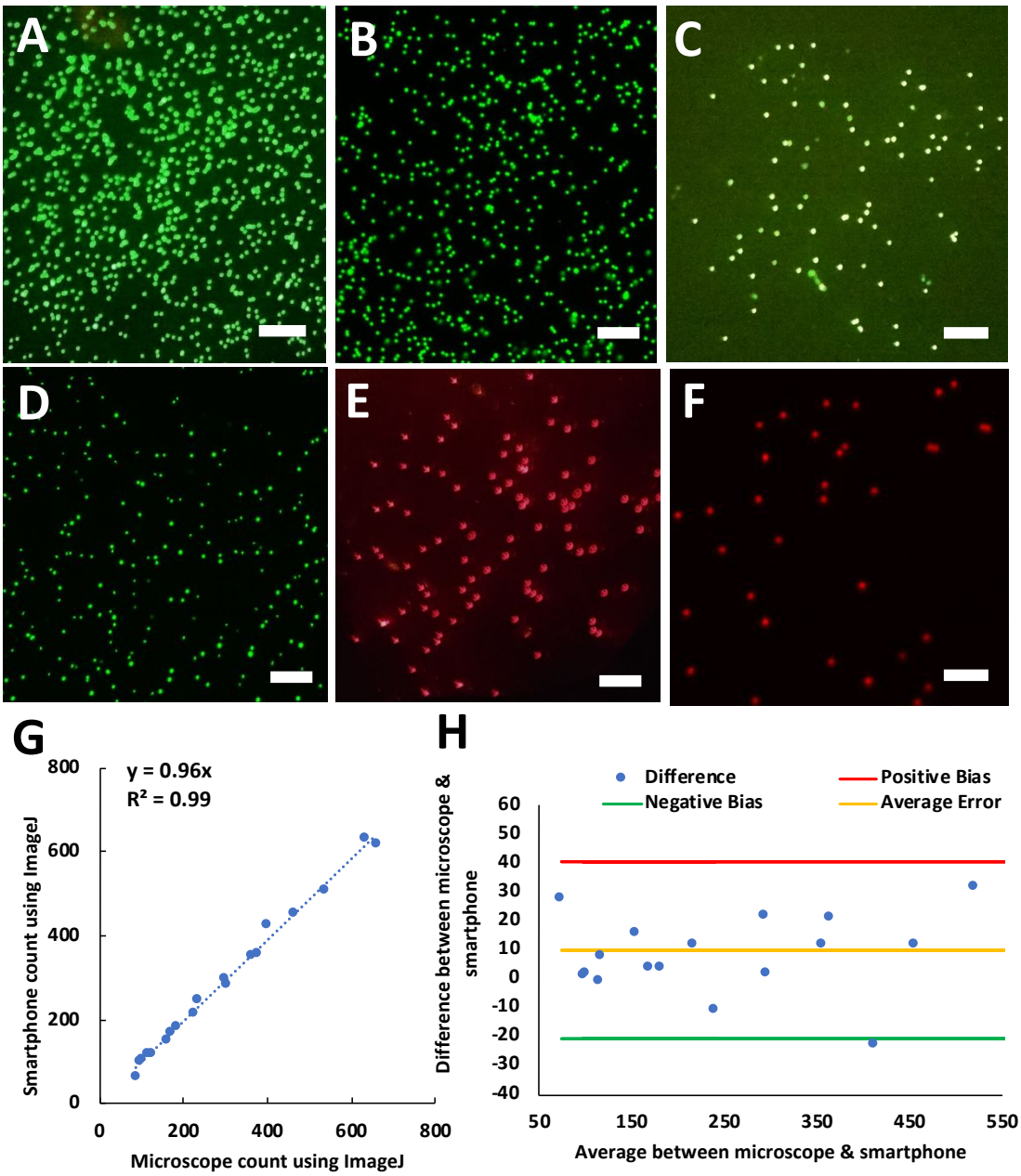

Figure 4: (A) Green fluorescent beads imaged from the designed SBFM and Galaxy S9+. (B) Green fluorescent beads imaged from a normal benchtop fluorescent microscope. (C) Leukocytes imaged from the designed SBFM and Galaxy S9+. (D) Leukocytes imaged from a normal benchtop fluorescent microscope. (E) Red fluorescent beads imaged from the designed SBFM and Galaxy S9+. (F) Red fluorescent beads imaged from a normal benchtop fluorescent microscope. (G) Correlation curve between SBFM count and microscope count using ImageJ. (H) Bland Altman analysis of the data resented in (C). (Scale bar = 100µm)

Multivariate regression using artificial neural networks:

We also analyzed the bead and leukocyte images obtained from the SBFM using the MATLAB based artificial neural networks. A two-layer feed-forward artificial neural network with 10 neurons for hidden layer and 1 neuron for output layer was used for the model. This network was then trained using different

data training algorithms including Levenberg Marquardt, scaled conjugate gradient, and Bayesian regularization. For each training method, ten networks were trained. Performance of these trained networks was then evaluated by a blinded testing images obtained from the SBFM and comparing their predicted counts to the control count obtained through ImageJ. **Table S2** lists the performance of each of these networks and showcases the average percentage error and the corresponding standard deviation. The best three performing neural networks were then picked for a closer evaluation and the resulting comparison plots between ANN counts and the control counts (ImageJ) are shown in **Figure 5**.

The first model was trained with scaled conjugate gradient method, and the corresponding error histogram and mean squared error (124.64) plots are shown in **Figure S6**. Hinton diagram representing the weight and bias values of all neurons in the hidden and output layers is shown in **Figure S7** and combined regression plot for training, validation, and testing data is shown in **Figure S8**. Additionally, the correlation plot between the ANN and ImageJ count is shown in **Figure 5A**, which shows a correlation of R^2= 0.99 and a slope of 0.88. The Bland Altman analysis of the same data is shown in **Figure 5B**, which shows the average error to be equal to 28.41 and the limits of agreement are (95.00, -38.17). The mean percentage error for this network was -9% with a standard deviation of 7.44%. The bias and the weight values of the neurons in the trained network are shown in **Table S3**. The second model was also trained with scaled conjugate gradient method, and the corresponding error histogram and mean squared error (217.72) plots are shown in **Figure S9**. Hinton diagram representing the weight and bias values of all neurons in the hidden and output layers is shown in **Figure S10** and combined regression plot for training, validation, and testing data is shown in **Figure S11**. Additionally, the correlation plot between the second ANN and ImageJ count is shown in **Figure 5C**, which shows a correlation of R^2= 0.99 and a slope of 0.89. The Bland Altman analysis of the same data is shown in **Figure 5D**, which shows the average error to be equal to 23.46 and the limits of agreement are (88.27, -41.33). The mean percentage error for this network was -6.31% with a standard deviation of 6.92%. The bias and weight values of the neurons in the trained network are shown in **Table S4**. The third model was trained with Bayesian regularization method, and the corresponding error histogram and mean squared error (3.99) plots are shown in **Figure S12**. Hinton diagram representing the weight and bias values of all neurons in the hidden and output layers is shown in **Figure S13** and combined regression plot for training, validation, and testing data is shown in **Figure S14**. Additionally, the correlation plot between the said ANN and ImageJ count is shown in **Figure 5E**, which shows a correlation of R^2= 0.99 and

a slope of 0.93. The Bland Altman analysis of the same data is shown in **Figure 5F**, which shows the average error to be equal to 13.71 and the limits of agreement are (92.36, -64.94). The mean percentage error for this network was -2.9% with a standard deviation of 13.65%. The bias and weight values of the neurons in the trained network are shown in **Table S5**. In **Table 1**, we have showcased the training and performance characteristics of the three artificial neural networks.

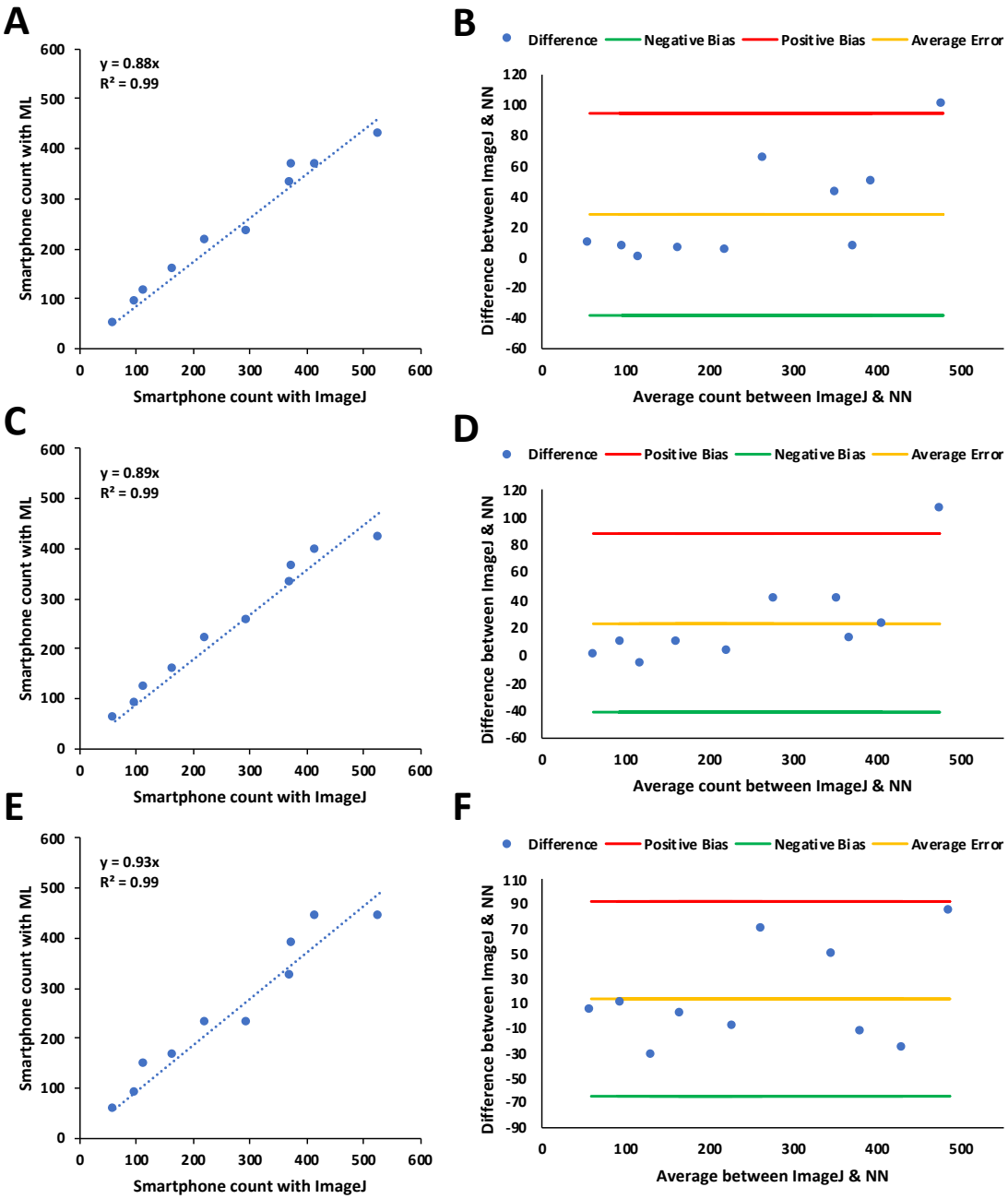

Figure 5: (A) Correlation curve between counts from NN1 (scaled conjugate gradient) and ImageJ. (B) Bland Altman analysis of the data presented in (A). (C) Correlation curve between counts from NN2 (scaled conjugate gradient) and ImageJ. (D) Bland Altman analysis of the data presented in (C). (E) Correlation

curve between counts from NN3 (Bayesian regularization) and ImageJ. (F) Bland Altman analysis of the data presented in (E).

		Neural network results		Linear regression, Bland-Altman analysis, & Percent Error					
	Method	R value	Mean squared error	R^2 value	Bland-Altman (mean error)	Bland-Altman (pos. bias)	Bland-Altman (neg. bias)	Error (%)	Standard deviation (%)
NN 1	SCG	0.99	124.64	0.99	28.41	95.00	-38.17	-9.04	7.44
NN 2	SCG	0.99	217.72	0.99	23.46	88.27	-41.33	-6.31	6.92
NN 3	BR	0.99	3.99	0.99	13.17	92.36	-64.94	-2.90	13.65

Table 1: Comparison between the performance of ImageJ (control) and the different methods used to train the artificial neural network for particle counting.

Statistical analysis:

Statistical analysis was performed using R to evaluate whether the counts predicted by the three ANN based algorithms deviated significantly from the ones obtained through control (ImageJ). The boxplots for all the particles count images from both control and the ANN model can be seen in **Figure 6A**. First, Shapiro-Wilk tests were performed to determine the normality of the data. The Shapiro-Wilk tests yielded the values: W=0.94691, p-value=0.6321 for ImageJ, W=0.93759, p-value=0.5266 for Scaled Conjugate Gradient 1 (SCG1 i.e., ANN model 1); W=0.93105, p-value=0.4583 for Scaled Conjugate Gradient 2 (SCG2 i.e., ANN model 2); and W=0.92748, p-value=0.4236 for Bayesian Regularization (BR i.e., ANN model 3). The high p-values in all the cases indicate that the data does not deviate significantly from normality. Next, we determined if the variances among the data sets are equivalent using Bartlett's test to assess if ANOVA could be performed. The Bartlett's test yielded a p-value = 0.9504, proving that the variances do not differ significantly. One-way ANOVA was subsequently performed and yielded the values (F-value=0.0792, p-value=0.9709), highlighting, there is no significant difference among the 4 populations. For better visualization, we also performed Tukey's Honestly Significant Difference (HSD) test for individual comparison of data sets and found no statistically significant difference among the sets as evident from **Figure 6**B.

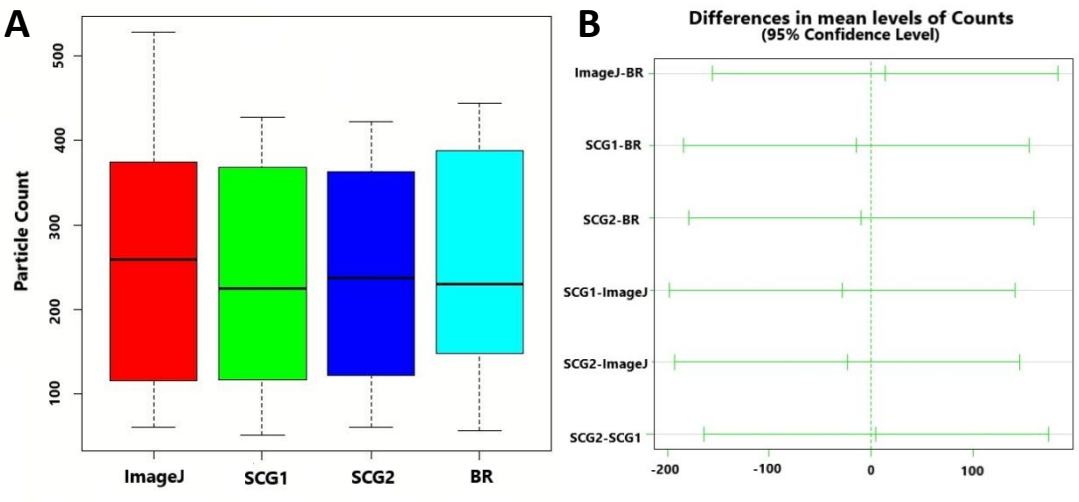

Figure 6: (A) Box plots of the particle count data sets obtained from control (ImageJ) and the ANN based algorithm. (B) Tukey plot of the data shown in (A).

Discussion

An ideal SBFM should offer multiple magnification options, ability to image multiple fluorophores, and flexibility of platform compatibility e.g., glass slides, microfluidic devices etc. Furthermore, owing to the extreme variety of smartphones, their camera specification and configurations being changed frequently, SBFMs should be capable of working with different smartphones to avoid frequent design changes. In **Table S6**, we have listed and compared our setup and previously reported SBFMs and the different functionalities offered by them. Our SBFM is the only design which successfully fulfils all the mentioned criteria overcoming their geometric and design limitations.

The different spatial resolution offered by Lumia 1020 and Samsung Galaxy S9+ with the SBFM is due to the different magnification ratios and pixel pitches of their respective camera sensors. At same magnification ratio, Lumia 1020 will always have a better spatial resolution because it has a higher pixel pitch. However, the spatial resolution offered by Galaxy S9+ is appropriate for leukocyte counting application as seen from the presented results. Moreover, it offers better connectivity, more functionality, and a higher computational power compared to the Lumia 1020. We can also increase spatial resolution with a Galaxy S9+ by using external lenses with smaller focal lengths to increase the magnification ratio to unity or even higher. There is however a limit to this, and eventually, the spatial resolution would be limited by the Rayleigh criteria

which states $R = \frac{0.61\lambda}{NA}$. The numerical aperture (NA) of Galaxy S9+ internal lens is about 0.34, when used in conjunction with an external lens of the same NA, this would translate into a resolution limit of about 987 nm when working with green fluorophores ($\lambda = 550$ nm), and about 1.12 µm when working with red fluorophores ($\lambda = 620$ nm).

The field of view (FOV) being offered by the SBFM is just as important as the magnification. With larger magnification results in smaller FOV and vice versa. The field of view offered by the SBFM depends on the ratio of the focal lengths of the external lens to the smartphones' lens along with the sensor size of the smartphone. Samsung Galaxy S9+ has a sensor size of about 5.76 x 4.29 mm and the focal length of its internal lens is 4.3 mm. Using Galaxy S9+ with lens A (15 mm focal length), results in magnification of 0.29 (4.3/15), and a FOV of about 19.86 x 14.79 mm. When lens B (10 mm focal length) is used, we get magnification of about 0.43 (4.3/10) and FOV of about approximately 13 x 10 mm. The ability to choose between having a larger field of view and a larger magnification is an important feature offered by our SBFM depending on the specific application requirements, imaging area, and particle concentrations etc. Our setup can be used to work between two different fluorophores at multiple magnification settings, however, user needs to replace the long pass filter in case of changing the fluorophore setting, or a different magnification level can be selected by swapping the appropriate lens.

The darkfield created by the combination of top and bottom portion of the SBFM is necessary for fluorescent microscopy. But in addition to that, it also helps in making the performance of SBFM consistent in different ambient lighting conditions by minimizing exposure of the sample to external ambient light. The only light that reaches the sample under consideration is from the SBFM's excitation LED's which is why the lighting condition always remains consistent. The SBFM can, therefore, be used in different ambient lighting conditions with high accuracy and consistency.

To automate the process of particle counting from the images obtained using the SBFM, we trained multiple neural networks based on different training algorithms. First, we used Levenberg Marquardt method, it takes more memory but less time to train and the training stops when there is no improvement in generalization which is also indicated by an increase in the mean squared error of samples. Second, we used scaled conjugate gradient method, it takes the least memory of all the methods and the training stops when there is no improvement in generalization, which is also indicated by an increase in the mean squared error of

samples. Lastly, we used Bayesian regularization method, it takes more time to train but offers better prediction accuracy and can be used for noisy datasets. In Bayesian regularization, training is stopped on the basis of a regularization protocol i.e., adaptive weight minimization.

The correlation graphs shown in **Figure 4** and **Figure 5** shows a good particle count correlation between control and SBFM. However, the low intercept values shown in **Fig.4G** and **Figs. 5A, 5C**, and **5E**, indicates the slight under-prediction. One of the possible reasons is the limited sample volume we used for this study i.e., particles were suspended in the droplets of 2 µl volume. Using higher particle concentrations in smaller volumes, multiple fluorescent particles may appear clustered together and result in underprediction of the counts compared a bigger benchtop fluorescent microscope with a higher optical resolution. One possible way to overcome challenge is to disperse the 2 µl sample over a larger surface area, which will reduce the clustering of particles and help in improving the efficacy of particle counts[29]. In addition, the accuracy can be further improved by using a lens with an even smaller focal length. This will increase the optical resolution of the SBFM, and thereby help resolve the clustered particles by the ANN's, resulting in an improved accuracy. The different focal length of the lens will also result in changing the effective field-of-view (FOV). Thus, the lens's focal length, FOV, and sample volume parameters should be selected based on a target application.

We used ImageJ as control particle counts. ImageJ is an established software that is used for the quantification of fluorescent particles imaged using different platforms in many laboratories. Though precise, analysis using ImageJ requires multiple manual processing steps such as thresholding and conversion of coloured images into grey scale. Furthermore, in terms of moving towards a complete end to end user product system, ImageJ presents significant difficulties in terms of scaling and implementation on a smartphone themselves. We therefore developed ANN based algorithm to quantify the fluorescent particles imaged by the SBFM.

The selection of the training algorithm for ANN depends on the processing time and the computational memory required. In our case we used 93 images for training, which is a smaller dataset and thus does not require any significant computational processing to train our models. The results obtained from ANOVA and Tukey's test indicate that the performance of the ANN based particle counting algorithms is comprabale to the control (ImageJ) which is also evident from the calculated p-values. The presented ANN based

algorithm relies on phase coding approach to identify and detect circles and has complexity ranging between (N^2 to N^4) [32]. The effect of the algorithms' complexity is clearly evident from the real-world processing times of the images obtained through multiple smartphones at different aspect ratios and magnification levels (**Table S7**). An interesting observation from **Table S7** is that the algorithm takes longer to process images which have been captured at a higher zoom level. This happens because magnification level is directly proportional to the pixel diameter of fluorescent particles being imaged. This results in increased computation because of the inherent nature of phase coding approach.

The presented SBFM along with the particle quantification algorithm can be used for a number of applications. Our SBFM is fully capable of working in conjunction with PDMS based microfluidic devices for the quantification of leukocytes at point of care as well[29]. By binding a different antibody in the microfluidic device, we can also image and quantify subtypes of leukocytes with specific antigen expressions such as nCD64[30].

Conclusions

We have presented the design of a modular SBFM that can be used for imaging multiple fluorophores, has multiple magnification options, and can be used with multiple smartphones. We imaged fluorescent polystyrene beads and human leukocytes with the presented SBFM and observed a good correlation between the performance of our SBFM and a regular benchtop microscope. Furthermore, we developed and trained multiple artificial neural networks to quantify the beads/leukocytes imaged using the SBFM and found no statistical difference in its performance compared to the control (ImageJ). Even though we have only imaged fluorescent beads and leukocytes in current study, the presented SBFM with ANN based counting algorithm can easily be used with microfluidic diagnostic and cell culture devices and can therefore reduce the dependency on expensive and bulky benchtop fluorescent microscopes.

Acknowledgements

Authors would like to acknowledge the funding support from Department of Electrical and Computer Engineering, Global Health Institute and Research Council at Rutgers, The State University of New Jersey. Authors also acknowledges funding support from National Science Foundation (Award number # 2002511), and Office of Naval Research (ONR) (DURIP award # N00014-20-1-2542).

Conflict of interest

The authors declare no conflicts of interest.

References

1. Tata, B.; Raj, B., Confocal laser scanning microscopy: Applications in material science and technology. *Bulletin of Materials Science* **1998,** *21* (4), 263-278.

2. Leung, B. O.; Chou, K. C., Review of super-resolution fluorescence microscopy for biology. *Applied spectroscopy* **2011,** *65* (9), 967-980.

3. Munné, S.; Grifo, J.; Cohen, J.; Weier, H., Chromosome abnormalities in human arrested preimplantation embryos: a multiple-probe FISH study. *American journal of human genetics* **1994,** *55* (1), 150.

4. Raj, A.; Van Den Bogaard, P.; Rifkin, S. A.; Van Oudenaarden, A.; Tyagi, S., Imaging individual mRNA molecules using multiple singly labeled probes. *Nature methods* **2008,** *5* (10), 877-879.

5. Zhu, W.; Gong, C.; Kulkarni, N.; Nguyen, C. D.; Kang, D., Smartphone-based microscopes. In *Smartphone Based Medical Diagnostics*, Elsevier: **2020**; pp 159-175.

6. Roda, A.; Michelini, E.; Zangheri, M.; Di Fusco, M.; Calabria, D.; Simoni, P., Smartphone-based biosensors: A critical review and perspectives. *TrAC Trends in Analytical Chemistry* **2016,** *79*, 317-325.

7. Ludwig, S. K.; Tokarski, C.; Lang, S. N.; van Ginkel, L. A.; Zhu, H.; Ozcan, A.; Nielen, M. W., Calling biomarkers in milk using a protein microarray on your smartphone. *PLoS One* **2015,** *10* (8), e0134360.

8. Ludwig, S. K.; Zhu, H.; Phillips, S.; Shiledar, A.; Feng, S.; Tseng, D.; van Ginkel, L. A.; Nielen, M. W.; Ozcan, A., Cellphone-based detection platform for rbST biomarker analysis in milk extracts using a microsphere fluorescence immunoassay. *Analytical and bioanalytical chemistry* **2014,** *406* (27), 6857-6866.

9. Coskun, A. F.; Nagi, R.; Sadeghi, K.; Phillips, S.; Ozcan, A., Albumin testing in urine using a smart-phone. *Lab on a Chip* **2013,** *13* (21), 4231-4238.

10. Wei, Q.; Luo, W.; Chiang, S.; Kappel, T.; Mejia, C.; Tseng, D.; Chan, R. Y. L.; Yan, E.; Qi, H.; Shabbir, F., Imaging and sizing of single DNA molecules on a mobile phone. *ACS nano* **2014,** *8* (12), 12725-12733.

11. Kühnemund, M.; Wei, Q.; Darai, E.; Wang, Y.; Hernández-Neuta, I.; Yang, Z.; Tseng, D.; Ahlford, A.; Mathot, L.; Sjöblom, T., Targeted DNA sequencing and in situ mutation analysis using mobile phone microscopy. *Nature communications* **2017,** *8* (1), 1-8.

12. Zhu, H.; Sencan, I.; Wong, J.; Dimitrov, S.; Tseng, D.; Nagashima, K.; Ozcan, A., Cost-effective and rapid blood analysis on a cell-phone. *Lab on a Chip* **2013,** *13* (7), 1282-1288.

13. Koydemir, H. C.; Gorocs, Z.; Tseng, D.; Cortazar, B.; Feng, S.; Chan, R. Y. L.; Burbano, J.; McLeod, E.; Ozcan, A., Rapid imaging, detection and quantification of Giardia lamblia cysts using mobile-phone based fluorescent microscopy and machine learning. *Lab on a Chip* **2015,** *15* (5), 1284-1293.

14. Wei, Q.; Qi, H.; Luo, W.; Tseng, D.; Ki, S. J.; Wan, Z.; Göröcs, Z. n.; Bentolila, L. A.; Wu, T.-T.; Sun, R., Fluorescent imaging of single nanoparticles and viruses on a smart phone. *ACS nano* **2013,** *7* (10), 9147-9155.

15. Sung, Y.; Campa, F.; Shih, W.-C., Open-source do-it-yourself multi-color fluorescence smartphone microscopy. *Biomedical optics express* **2017,** *8* (11), 5075-5086.

16. Dai, B.; Jiao, Z.; Zheng, L.; Bachman, H.; Fu, Y.; Wan, X.; Zhang, Y.; Huang, Y.; Han, X.; Zhao, C., Colour compound lenses for a portable fluorescence microscope. *Light: Science & Applications* **2019,** *8* (1), 1-13.

17. Cho, S.; Islas-Robles, A.; Nicolini, A. M.; Monks, T. J.; Yoon, J.-Y., In situ, dual-mode monitoring of organ-on-a-chip with smartphone-based fluorescence microscope. *Biosensors and Bioelectronics* **2016,** *86*, 697-705.

18. Lee, S. A.; Yang, C., A smartphone-based chip-scale microscope using ambient illumination. *Lab on a Chip* **2014,** *14* (16), 3056-3063.

19. Meng, X.; Huang, H.; Yan, K.; Tian, X.; Yu, W.; Cui, H.; Kong, Y.; Xue, L.; Liu, C.; Wang, S., Smartphone based hand-held quantitative phase microscope using the transport of intensity equation method. *Lab on a Chip* **2017,** *17* (1), 104-109.

20. Jung, D.; Choi, J.-H.; Kim, S.; Ryu, S.; Lee, W.; Lee, J.-S.; Joo, C., Smartphone-based multi-contrast microscope using color-multiplexed illumination. *Scientific reports* **2017,** *7* (1), 1-10.

21. Müller, V.; Sousa, J. M.; Koydemir, H. C.; Veli, M.; Tseng, D.; Cerqueira, L.; Ozcan, A.; Azevedo, N. F.; Westerlund, F., Identification of pathogenic bacteria in complex samples using a smartphone based fluorescence microscope. *RSC advances* **2018,** *8* (64), 36493-36502.

22. Knowlton, S.; Joshi, A.; Syrrist, P.; Coskun, A. F.; Tasoglu, S., 3D-printed smartphone-based point of care tool for fluorescence-and magnetophoresis-based cytometry. *Lab on a Chip* **2017,** *17* (16), 2839-2851.

23. Y. Shan, B. Wang, H. Huang, D. Jian, X. Wu, L. Xue, S. Wang and F. Liu, Biosensors and Bioelectronics, **2019**, 132, 238-247.

24. C. Song, Y. Yang, X. Tu, Z. Chen, J. Gong and C. Lin, IEEE Sensors Journal, **2021**, 21, 1229-1235.

25. K. de Haan, H. Ceylan Koydemir, Y. Rivenson, D. Tseng, E. Van Dyne, L. Bakic, D. Karinca, K. Liang, M. Ilango, E. Gumustekin and A. Ozcan, npj Digital Medicine, **2020**, 3.

26. W. Zhu, G. Pirovano, P. O'Neal, C. Gong, N. Kulkarni, C. Nguyen, C. Brand, T. Reiner and D. Kang, Biomedical Optics Express, **2019**, 11, 89.

27. S. Chung, L. Breshears, A. Gonzales, C. Jennings, C. Morrison, W. Betancourt, K. Reynolds and J. Yoon, Nature Protocols, **2021**.

28. S. Talebian and M. Javanmard, Talanta, **2021**, 228, 122244.

29. Sami, M. A.; Wagner, K.; Parikh, P.; Hassan, U. In *Smartphone Based Microfluidic Biosensor for Leukocyte Quantification at the Point-of-Care*, 2019 IEEE Healthcare Innovations and Point of Care Technologies,(HI-POCT), IEEE: **2019**; pp 119-122.

30. Ghonge, T.; Koydemir, H. C.; Valera, E.; Berger, J.; Garcia, C.; Nawar, N.; Tiao, J.; Damhorst, G. L.; Ganguli, A.; Hassan, U., Smartphone-imaged microfluidic biochip for measuring CD64 expression from whole blood. *Analyst* **2019,** *144* (13), 3925-3935.

31. Fan, Y.; Yang, C., Competition, Product Proliferation, and Welfare: A Study of the US Smartphone Market. *American Economic Journal: Microeconomics* **2020,** *12* (2), 99-134.

32. Smereka, M.; Dulęba, I., Circular object detection using a modified Hough transform. *International Journal of Applied Mathematics and Computer Science* **2008,** *18* (1), 85-91